Urban ventilation assessment with improved vertical wind profile in high-density cities – Investigations in nighttime extreme heat

Yueyang He [1, 2], Chao Yuan [3, *], Chao Ren [4], Weiwen Wang [5, 6], Yuan Shi [1], Edward Ng [1, 2, 7]

1. Institute of Future Cities, The Chinese University of Hong Kong, Hong Kong, China
2. Institute of Environment, Energy and Sustainability, The Chinese University of Hong Kong, Hong Kong, China
3. Department of Architecture, National University of Singapore, Kent Ridge, Singapore
4. Division of Landscape Architecture, Faculty of Architecture, The University of Hong Kong, Hong Kong, China
5. Institute for Environmental and Climate Research, Jinan University, Guangzhou, China
6. Guangdong-Hong Kong-Macau Joint Laboratory of Collaborative Innovation for Environmental Quality, Guangzhou, China
7. School of Architecture, The Chinese University of Hong Kong, Hong Kong, China

* Corresponding author. Email address: akiyuan@nus.edu.sg

Abstract

Climate change and heatwaves challenge urban dwellers' thermal comfort and public health. In Hong Kong, more frequent and intensive extreme heat has been observed recently. This study uses Light Detection and Ranging (LiDAR) to observe vertical wind profiles and calibrate numerical simulation methods for urban ventilation assessment in nighttime extreme heat (i.e. hot nights (HNs)) at a typical high-density urban site. A cross-comparison is conducted to the shape characteristics between the observed HN-averaged wind profiles and conventionally-used 24-hour-averaged wind profiles in summer. The observation reveals a weaker wind environment in HNs than 24-hour-periods, and the weakest condition is found in HNs during prolonged extreme heat. Furthermore, CFD simulations are conducted to evaluate the deviations on urban ventilation assessment caused by the lack of consideration of nighttime extreme heat when setting the inlet wind profiles and site thermal conditions. In the simulation results, the 24-hour-averaged wind profiles cause significant deviations on pedestrian-level wind speed and velocity ratio (empirical model (> 45%); LiDAR observation (> 20%)). Considerable deviations are found when unstable thermal stratification is ignored (> 20%). Consistent deviations on vertical turbulent flow structures induced by the inexplicit coupling between thermal buoyancy and advection are found. The findings call for urgent attention to the wind conditions in HNs since they are most needed for releasing heat stress and cooling down the overheating at urban areas. The findings also suggest the need for LiDAR observational data, preferably considering extreme heat, to optimize urban ventilation assessment for tackling extremely high-temperature and weak-wind conditions.

Keywords

Heatwave; Vertical wind speed profile; Urban ventilation; High-density city; Doppler LiDAR; CFD

1. Introduction

1.1. Background

In tropical and subtropical climates, urban ventilation is important to human thermal comfort and health [1, 2]. A previous study has suggested that every 1 m/s increase in wind speed can mitigate a 2°C rise in urban air temperature in summer [3]. However, the urban wind environment is sensitive to its surrounding morphological features, especially in high-density cities [4, 5]. Thus, continuous efforts have been made in high-density cities to establish and optimize urban ventilation assessment tools and relevant urban planning/design guidelines for designing a better-ventilated city and solving the weak-wind-related environmental problems [6-8].

The recent trend of global climate change presents a new challenge to urban ventilation assessment. According to the latest report of the Intergovernmental Panel on Climate Change (IPCC) in 2021 [9], the global land surface temperature is successively higher in each of the last four decades, reaching a total increment of 1.59°C [9] in 2011 – 2020 in respect to 1850 – 1900. It is virtually certain that extreme heat, including heatwaves, have clearly discernible increases in their frequency and intensity on most of the land regions. They have been regarded as one of the major causes of heat-related mortality worldwide [10-14]. Worse still, cities intensify human-induced warming locally, and urbanization consequently increases the severity of these extreme heat [15-17]. Under this circumstance, a better understanding on how the wind behaves in extreme heat is required to support accurate urban ventilation assessment when the wind is most needed for heat-stress relief. Yet, the progress so far is hindered by the lack of field observation data and the complex heat-wind interactions in urban boundary layers [18].

1.2. A "new normal" in Hong Kong

As one of the most representative high-density cities, Hong Kong suffers from high-temperature and weak-wind conditions in summer. Additionally, in line with the recent trend of global climate change, Hong Kong Observatory (HKO) has observed a local temperature rise, which is faster than the global one [19]. Such changing climate has consequentially led to a substantial increase in local extreme heat, which can be identified by hot nights (HNs: daily minimum air temperature ≥ 28°C [20]) and very hot days (HDs: daily maximum air temperature ≥ 33°C [21]). For example, the number of HNs in the summer months (i.e. 1 June to 31 August) has gone up by 3 times from 2000 to 2020, as shown in Fig. 1a. During the two decades, a total 45 HNs in maximum have been identified in summer 2020 (Fig. 1b), constituting half of the entire summer. This upward increasing trend of extreme heat is expected to continue in the foreseeable future [22].

As extreme heat has become a "new normal" in Hong Kong, their impacts have aroused an emerging concern of local urban climate and heat-related mortality. In a long-term study conducted by Ren et al. [23], extreme heat can enhance the typical Urban Heat Island (UHI) effects in Hong Kong by a 1.7°C rise in intensity and a 59% increase in duration. With the enhanced UHI effects, the weak wind conditions in high-density cities tend to contribute more to higher mortality, as revealed by Goggins et al. [24]. Furthermore, extreme heat at nighttime was found to have stronger associations with excess mortality than those at the daytime [25, 26]. Particularly, Wang et al. [26] attributed the highest mortality risks to prolonged extreme heat. Meanwhile, Shi et al. [27] investigated the spatial variability of extreme hot weather conditions in Hong Kong. Their regression models addressed the importance of urban ventilation for mitigating extreme heat, especially at the nighttime. The above findings suggest an urgent need of attentions to wind conditions in the "new normal" in Hong Kong, as well as a critical review on relevant urban ventilation assessment and wind-adaptive urban planning/design.

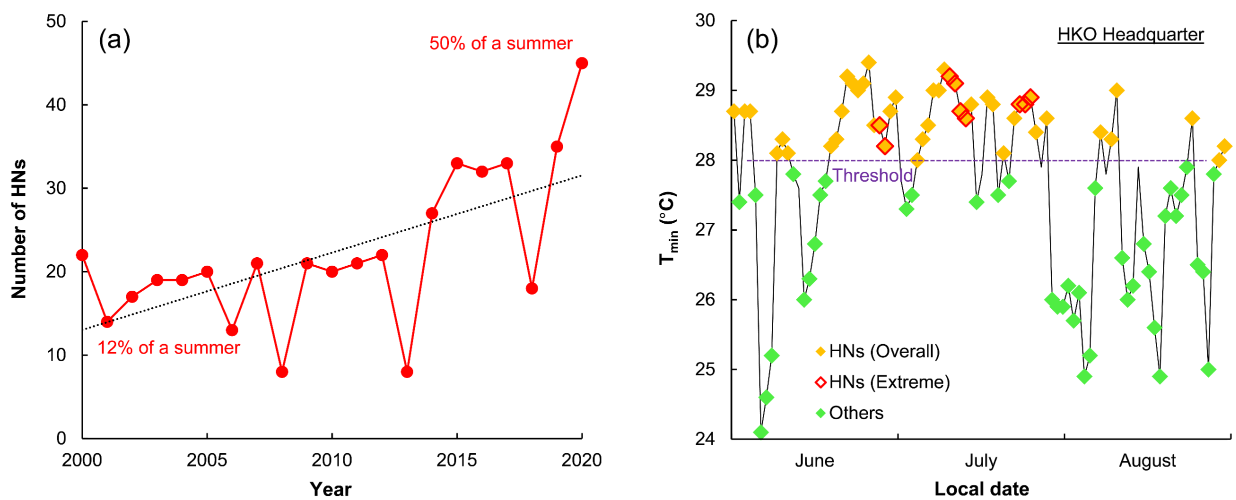

Fig. 1. Statistics of hot nights (HNs) in Hong Kong: (a) number of HNs in summer from 2000 to 2020; and (b) distribution of HNs in summer 2020 for overall situation (i.e. all HNs in summer 2020) and extreme situation (i.e. HNs in prolonged extreme heat as explained in Section 3) (source: HKO headquarter [19]).

1.3. Research gaps and objectives

To address weak-wind-related urban problems and guide wind-adaptive urban planning/design, the Planning Department, Hong Kong SAR Government has established the Air Ventilation Assessment (AVA) system since 2006 [8]. AVA provides a systematic methodology to assess pedestrian-level wind conditions using either wind tunnel or Computational Fluid Dynamics (CFD) simulations. This methodology has been used in all major developments in Hong Kong [28], and applied into other high-density cities [29-32]. However, the AVA system needs a critical review and update since its existing vertical wind profile dataset, named "site wind availability data" [33], has two main limitations. Firstly, this dataset was developed by wind tunnel and mesoscale meteorological modeling, and has not been validated by field observation. Secondly, this dataset does not take into account the "new normal" wind conditions in summer. Particularly, a standard AVA test currently adopts 24-hour-averaged wind data in either annual or seasonal extracts in this dataset to reproduce inflow boundary conditions regardless of extreme or non-extreme hot weather conditions. However, a refinement of the dataset is needed to tackle the increasingly frequent and intense extreme heat such as HNs, where the wind is most needed for relieving heat-stress and potentially reducing heat-related mortality risks.

Based on Light Detection and Ranging (LiDAR) observation of vertical urban wind speed profiles, which is introduced in Section 2, this study aims to address the above two limitations. There are two parts of the study. Part A (another paper [34]) is conducted to address the first limitation, i.e. lack of validation, by evaluating the accuracy of wind profiles estimated by conventional methods, including physical models (i.e. wind tunnel), mesoscale meteorological models, and empirical models (e.g. Power Law (PL)). Part B (the current paper) is conducted to address the second limitation, i.e. lack of consideration of extreme heat in summer, by two steps. Firstly, it cross-compares the "new normal" (i.e. HN-averaged) and normal (i.e. 24-hour-averaged) wind profiles. Secondly, it evaluates the impacts of these wind profiles on the CFD-based thermally-stratified urban ventilation assessment results. Specifically, the HN-averaged LiDAR wind profiles are used as a benchmark for assessing the deviations caused by the 24-hour-averaged wind profiles reproduced by LiDAR observation or a conventional method. The PL method is selected as the conventional method to be evaluated since it is the optimal alternative to LiDAR observation to estimate neutrally-stratified wind profiles in Part A [34].

2. Literature Review on Urban Wind Studies in Extreme Heat

Extreme heat are periods that trapped by abnormal warm air induced by synoptic-scale anticyclones [35]. Compared with non-extreme hot weather conditions in summer, extreme hot weather conditions further exacerbate the urban climate due to the amplified net radiation gain, increased anthropogenic heat, increased heat storage, decreased evapotranspiration, and decreased turbulent heat transport [36-39]. As one of the most complex urban climatic variables, wind in extreme heat is relatively weak due to the high-pressure circulation patterns under anticyclones [40]. Its behaviors have been increasingly studied by both field measurements and numerical simulations in recent years.

Based on conventional near-ground field measurements, a number of studies have revealed the positive contribution of wind to the synergies between heatwaves and urban heat island (UHI) effects [41-43]. For example, in a study in Beijing during heatwaves, Li et al. [44] found that wind played different roles in the synergies during the daytime and nighttime. They suggested that wind speed had a stronger impact on the sensible heat flux in urban areas than the advection cooling effect from the rural areas during the daytime, while an opposite trend occurred during the nighttime. In a study in Seoul, Ngarambe et al. [45] found that UHI is more intense during heatwaves than non-heatwave, and these synergies between heatwaves and UHI were more obvious in densely built areas and under low wind speed conditions. In another study in Hong Kong, Zhang et al. [46] found that a larger background wind speed was associated with a faster increase in daily maximum air temperature at coastal urban areas during extreme heat.

More recently, the development of ground-based remote sensing technologies, such as wind LiDAR, provides a new and reliable method to measure vertical wind speed profiles in hot periods. For example, Wu et al. [47] launched a LiDAR observation on the upper-air wind behaviors in extreme heat at the metropolitan area of New York City. Their study presented a strong diurnal variation of boundary layer heights during heatwaves, as well as its associations with the transport of urban air pollution. Based on multi-point LiDAR, He et al. [48] observed the diurnal variation of summer vertical wind speed profiles in Hong Kong. Their results confirmed a stronger buoyancy effect on the near-ground wind at the urban area with higher building density.

As for numerical simulations, mesoscale meteorological modeling has been widely used to predict urban surface wind and temperature in extreme heat [49-51]. As revealed by Li and Bou-Zeid [52], the low wind speed, together with the lack of surface moisture in urban areas, contributed the most to the enhanced UHI effects during extreme heat. Zhang et al. [53] quantified that the UHI effects can be reduced by over 25% during a heatwave if the upwind urban areas were replaced by natural vegetation in their simulations. Wang et al. [54] identified the different UHI circulation patterns over Beijing-Tianjing-Bebei region between the daytime and nighttime in the simulations. Furthermore, to understand the high-pressure atmospheric system induced by the UHI effects, Wang et al. [55] simulated the air circulation patterns under various background wind speed, heat flux and stratification conditions.

In microscales, CFD techniques have been widely used to simulate buoyancy-driven flow [56-58]. For example, based on unsteady Reynolds-averaged Navier-Stokes (URANS) and Large Eddy Simulation (LES) models, Mei and Yuan [59] investigated the merging of thermal plumes in an urban area of Singapore in calm conditions and attributed this phenomenon to both mean horizontal flow induced by pressure difference and turbulence induced by shear instability. Mei and Yuan [60] further conducted a literature review on buoyancy effects on urban ventilation, with a particular focus on strong buoyancy and weak wind conditions. Based on LES models, Wang et al. [61] investigated the coupled effects of mechanical and thermal turbulence with urban settings in Hong Kong and found that thermal turbulence enhanced pedestrian-level ventilation while thermal mixing was suppressed by high background wind speed. Besides, a few recent CFD studies have taken into account the near-ground wind and thermal conditions in extreme heat. Amongst these studies, Toparlar et al. [39] used URANS models to analyze the effects of wind speed on urban surface temperature in Bergpolder Zuid during a heatwave. Antoniou et al. [62] conducted a validation study between URANS models and field measurements in terms of near-ground wind speed and temperature in four consecutive days of a heatwave in Nicosia.

Despite these studies, however, few studies have investigated the vertical wind distribution in extreme heat, especially at high-density urban areas. The lack of such understanding may lead to deviations on inflow boundary conditions in urban ventilation assessment in extreme heat, which finally results in mistaken assessment outputs and wrong decision making in urban planning/design.

3. Reproduction of Vertical Urban Wind Profiles at Upwind

This section reproduces the abovementioned 24-hour-averaged and HN-averaged vertical wind speed profiles in summer. A typical high-density urban site in Sai Wan, Hong Kong is selected as an example to reproduce the wind profiles. As shown in Fig. 2, the selected site is located at a downtown area of northwestern Hong Kong Island. It is characterized by inhomogeneous high-rise buildings and limited open spaces. Fig. 3 shows the spatial distribution of building heights at the site, where the maximum building height is around 180 m, and the ground coverage ratio is over 40%. The selected site has a relatively flat terrain, while mountains on the south bind it.

Fig. 2. The selected high-density urban site (800 m × 800 m) in Sai Wan, Hong Kong for reproducing vertical wind speed profiles, and the wind LiDAR location on top of the roof of Yam Pak building (15 m above the ground).

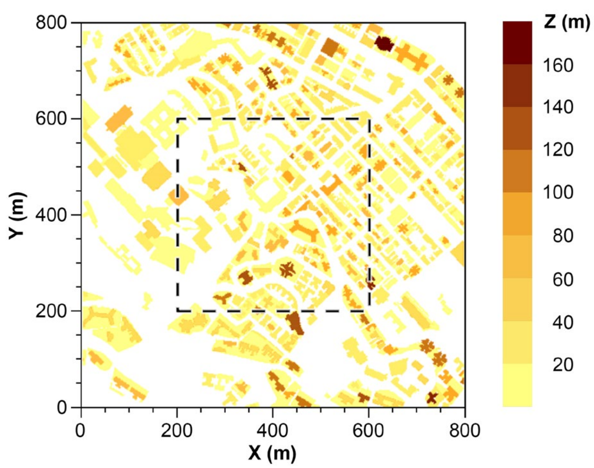

Fig. 3. Spatial distribution of building heights at the selected urban site in Sai Wan, Hong Kong.

The 24-hour-averaged and HN-averaged vertical wind speed profiles were reproduced by the following equations:

$$U_{\overline{24H}} = \frac{\sum_{i=1}^{m} U_{24H\_i}}{m} \qquad (1)$$

$$U_{\overline{HN}} = \frac{\sum_{i=1}^{n} U_{HN\_i}}{n} \qquad (2)$$

where $U_{\overline{24H}}$ and $U_{\overline{HN}}$ refer to the HN-averaged and 24-hour-averaged wind speed at different heights (*Z*), respectively; U_{24H_i} and U_{HN_i} refer to the hourly-averaged wind speed in each 24-hour-period and HN at *Z*, respectively; and *m* and *n* refer to the number of the identified 24-hour-periods and HNs during a study period, respectively. In this paper, following the AVA technical circular [28], $U_{\overline{24H}}$ was calculated by considering all 24-hour-periods in summer regardless of extreme or non-extreme hot weather conditions. In comparison, $U_{\overline{HN}}$ was calculated by considering all 45 HNs, as identified in Fig. 1b, in summer 2020 in an overall situation. Additionally, $U_{\overline{HN}}$ was also calculated in an extreme situation by extracting 9 HNs (Fig. 1b) in the middle of prolonged extreme heat in a pattern of 2D3N (i.e. 3 consecutive HNs with 2 HDs in between) in summer 2020, as 2D3N has the strongest association with the amplified mortality risks among different patterns of prolonged extreme heat in Hong Kong [26]. The reproduction of the hourly-averaged vertical wind speed profiles was based on LiDAR observation or conventional PL method, with further explanations in Sections 3.1 and 3.2.

3.1. LiDAR vertical urban wind profiles

The LiDAR method was based on a continuous field observation of vertical wind speed profiles on the roof-top of Yam Pak building in Hong Kong University at the selected site, as shown in Fig. 2. From the wind LiDAR, laser beams were emitted and received cyclically to detect the Doppler shifts (Δf) of the moving aerosol particles in the atmosphere:

$$\Delta f = f - f_0 \qquad (3)$$

where f_0 refers to the frequency of the emitted laser beams, and f refers to the frequency of the laser beams backscattered by the particles. The radical wind speed at each height was calculated proportionally to the detected Δf, and then converted into the corresponding wind speed. In this paper, the Doppler Beam Swinging (DBS) scan mode was used to reproduce the hourly-averaged LiDAR wind speed profiles:

$$U = \frac{\sqrt{(V_{RE} - V_{RW})^2 + (V_{RN} - V_{RS})^2}}{2 \sin \gamma} \qquad (4)$$

where V_{RE}, V_{RW}, V_{RN} and V_{RS} refer to the radial wind speed along the east-tilted, west-tilted, north-tilted and south-tilted directions detected at each height above the test site (Fig. 2) in a DBS scan circle; and γ refers to the half cone angle. The observational data in summer 2020 was extracted in the prevailing southwest wind direction (i.e.,$180° \leq \theta \leq 270°$) during non-typhoon periods. The extracted data was used to reproduce both the 24-hour-averaged and HN-averaged wind profiles. Detailed settings of the wind LiDAR are listed in Table 1. On-site validation results of the wind LiDAR conducted at the King's Park meteorological station in Hong Kong based on the upper-air data from radiosondes [63] are shown in Appendix A.

Table 1. Settings of wind LiDAR for observing the vertical wind speed profile in summer 2020.

Instrument condition	**Detailed setting**
LiDAR model	WindCube 100S
Scan mode	Doppler beam swinging (DBS)
Scan range	50 m to 3 km above the scanner
Scan cycle	Approximately 20s
Range gate (i.e., discrete interval)	25 m
Half cone angle	15°
Laser beams wavelength	1.54 μm
Carrier-to-noise ratio	-27 dB [48]
Measurement accuracy	0.5 m/s of radial wind speed at the range between 0 and 115 m/s [64]

3.2. Power law vertical urban wind profile

The conventionally-used PL method reproduced the vertical wind speed profiles by integrating the site wind availability data [33] developed by Regional Atmospheric Modeling System (RAMS) modeling with the power law empirical formula as suggested in the AVA technical circular [28]. In this hybrid method, the site wind availability data provides the reference wind speed above a test site and the power law formula determines the shape of its wind profile. In this paper, the hourly-averaged PL wind speed profiles were extrapolated as:

$$U = U_\infty \left(\frac{Z}{Z_\infty}\right)^a \qquad (5)$$

where U_∞ refers to the reference wind speed at the height of 500 m (Z_∞) from the computational cell (0.5 km x 0.5 km) covering the selected urban site (Fig. 2) in the RAMS dataset; and α refers to the power-law index where 0.35 was assigned to represent the terrain roughness of a city center according to the widely-used AIJ recommendations [65]. Currently, only 24-hour-averaged reference wind data in either annual or seasonal extracts are available in the RAMS dataset. Hence, this paper used the reference wind data in summer extract under the sector of southwest wind direction to reproduce the 24-hour-averaged wind profile. Detailed settings of the RAMS model for developing the site wind availability data are listed in Table 2.

Table 2. Settings of RAMS model [66] for developing the site wind availability data.

Model condition	**Detailed setting**

Mesoscale model	RAMS (version 6.0)
Horizontal data resolution	12.5 km (outermost); 2.5 km (middle); 0.5 km (innermost)
Simulation time	Year 2000 – 2009
Topography	Actual terrain height
Land surface types	Land-use data in a latitude/longitude resolution of 400'' (outermost); 80'' (middle); and 16'' (innermost)
Nudging	Near-ground wind and temperature data from local automatic weather stations [19]

3.3. Cross-comparison of 24-hour-averaged and HN-averaged vertical urban wind profiles

The 24-hour-averaged and HN-averaged vertical wind speed profiles in summer are plotted together for a cross-comparison in Fig. 4. The LiDAR observation shows smaller wind speed in HNs, i.e. LiDAR(HN), than 24-hour-periods, i.e. LiDAR(24H), suggesting the needs of additional attentions to the weak wind conditions in nighttime extreme heat. Particularly, obviously smaller background wind speed (as indicated by U_∞) is observed in HNs in the extreme situation (II) than the overall situation (I). This phenomenon can be caused by the weaker advection under stronger high-pressure circulation patterns in prolonged extreme heat. In such situations, urban thermal environment is exacerbated by the more lasting heat-stress while this heat-stress can be trapped inside street canyons for a longer time due to the weaker incoming wind speed [67]. Furthermore, the LiDAR results confirm the strong heat-wind interactions within the urban boundary layer over a high-density urban site as the wind profiles' shapes vary significantly under different buoyancy effects. The strongest buoyancy effect is observed in the weakest wind condition, i.e. LiDAR(HN)-II, which is consistent with the previous findings [60]. However, these highly variable buoyancy-induced flow behaviors in the reality cannot be accurately described by the PL wind profile, i.e. PL(24H).

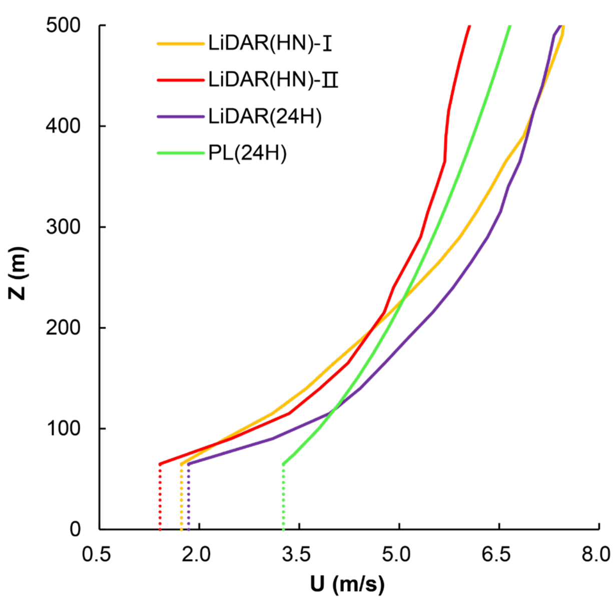

Fig. 4. Vertical wind speed (*U*) profiles reproduced by LiDAR observation and conventional power law (PL) method in hot nights (HNs) or 24-hour-periods (24Hs) in summer.

4. CFD Simulations

Based on the wind profiles reproduced in Section 3, this section used the LES model in an open-source CFD code, Parallelized LES Model (PALM) version 6.0, to conduct urban ventilation assessment. The LES model relies on filtered and incompressible Navier-Stokes equations in Boussinesq-approximated form [68], and explicitly resolves large and energy-containing eddies. A validation of the LES model based on wind tunnel experimental data has been conducted in Part A [34], and the validation result is attached in Appendix B.

4.1. Definition of test scenarios in CFD

Four test scenarios were defined respectively in the overall (I) and extreme (II) situations, which included a benchmark scenario and three scenarios to be evaluated (Table 3). The benchmark scenario considered nighttime extreme hot weather conditions when setting both inlet wind profiles, i.e. HN-averaged LiDAR wind profiles (LiDAR(HN)); and site thermal conditions, i.e. unstable thermal conditions (U) determined by field measurements. For comparison, the other scenarios did not specify nighttime extreme hot weather conditions in inlet wind profiles, i.e. 24-hour-averaged PL or LiDAR wind profiles (PL(24H) or LiDAR(24H)); or site thermal conditions, i.e. neutral thermal condition (N). Methods to set the inlet wind profiles and site thermal conditions in CFD are described in Sections 4.2 and 4.3, respectively.

Table 3. Test scenarios with different input parameters for CFD simulations.

Scenarios	Methods	Periods	Thermal conditions	Situations
LiDAR(HN)-U-I/II	LiDAR	Hot nights (HNs)	Unstable (U)	Overall (I)
PL(24H)-U-I/II				
LiDAR(24H)-U-I/II	PL	24-hour-periods (24Hs)	Neutral (N)	Extreme (II)
LiDAR(HN)-N-I/II				

Note: total eight test scenarios are involved with different combinations of four pairs of alternative input parameters, where "methods" and "periods" prescribe inlet wind profiles; "thermal conditions" prescribe site thermal conditions; and "situations" determine the effects of HNs on both inlet wind profiles and site thermal conditions.

4.2. Settings of computational domain, grids and flow boundary conditions

Following the settings of the LES model in Part A [34], the computational domain had a size of 2800 m (X) × 800 m (Y) × 500 m (Z), as shown in Fig. 5. The computational gird was structured with a total cell number of 1400 (X) × 400 (Y) × 120 (Z), where the cell size was 2 m with no stretching ratio in the horizontal dimension and 1 m with a stretching ratio of 1.03 beyond the height of 25 m in the vertical dimension. This grid resolution was determined by a grid-sensitivity test conducted by Gronemeier et al. [69] in PALM, based on a high-density urban model, to best compromise simulation accuracy and computational cost.

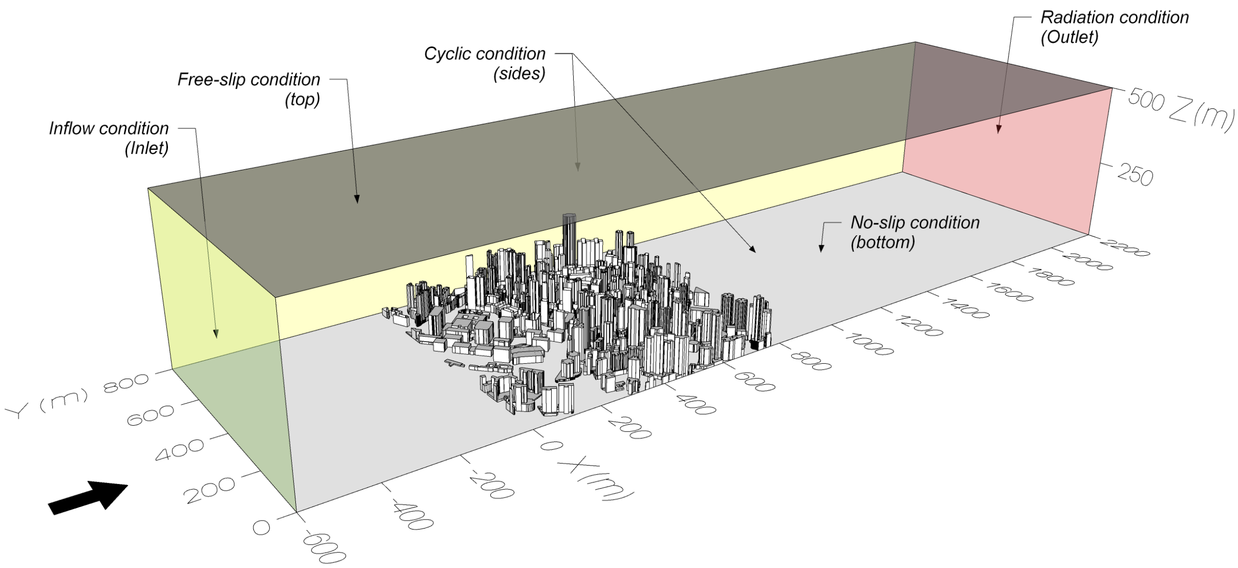

Fig. 5. Computational domain and boundary conditions of the LES model with a high-density urban model.

In the computational domain, the inlet boundary adopted a dirichlet condition, where the vertical wind speed profiles reproduced in Section 3 were prescribed. To have a fair cross-comparison, this paper only prescribed the vertical wind speed profiles within the overlap range of the LiDAR and PL methods, which is from 65 m above the ground till 500 m. Below the height of 65 m, the wind speed in either method was prescribed to be constant. It assumed that the wind speed gradient inside urban canopies is negligible below the displacement height until quite close to the ground surface, referring to the descriptions in the reality by Bentham and Britter [70], and Oke [71]. Based on prescribed vertical wind speed profiles, the initial turbulence was generated by the synthetic turbulence generator [72], where the instantaneous wind speed component (u_i) at the inlet was calculated at each time step (*t*) by the following equation:

$$u_i(t) = \bar{u}_i(t) + \alpha_{ij}(t) u'_j(t) \quad (6)$$

where $i, j \in [1, 2, 3]$; $\bar{u}_i$ refers to a mean wind speed component; α_{ij} refers to an amplitude tensor derived from the Reynolds stress tensor, which was parametrized automatically by the method of Rotach et al. [73] in PALM; and u'_j refers to the turbulent motions, which were obtained by the following equation:

$$u'_j(t) = u'_j(t - \Delta t) exp\left(\frac{-\pi\Delta t}{2T}\right) + \psi_j(t - \Delta t)\left[1 - exp\left(\frac{-\pi\Delta t}{T}\right)\right]^{0.5} \quad (7)$$

where ψ_j refers to a set of random data generated independently in PALM at each time step, with a zero mean and a unity variance; Δt refers to the interval of 1 time step; and *T* refers to the Lagrangian time scale.

The outlet boundary adopted a radiation condition. The bottom, top and lateral boundaries adopted no-slip, free-slip and cyclic condition, respectively. The total simulation time for each scenario was 1.5 hours, where the simulation result in the last half hour was averaged and outputted. Automatic adjustment of the time step is set to guarantee the courant number less than 1.

4.3. Settings of urban thermal conditions

The LES model adopts either neutral or unstable thermal conditions to address the impacts of thermal buoyancy at the test urban site. In the test scenarios with a neutral thermal condition, the calculation of heat transfer was switched off. In the test scenarios with unstable thermal conditions, initial air temperature and surface heat flux in CFD were determined by field measurements. The initial air temperature in HNs was reproduced by averaging the air temperature observed at HKO headquarter [19] in HNs in summer 2020. Specifically, the overall and extreme situations, as defined in Section 3, averaged the maximum air temperature in all 45 HNs (30.1°C) in summer and 9 HNs in prolonged extreme heat (30.6°C), respectively. The surface heat flux was reproduced according to the field measurement data obtained at Yam Pak building (Fig. 2) by Yang and Li [74]. Fig. 6 shows the diurnal variations of surface temperature measured on the building roof and walls by thermal couples, and air temperature measured by a weather station on the building roof from 24 to 25 July in summer 2008. The measured minimum air temperature at these two days is close to 28°C, which is the threshold [20] to define a HN. Since a similar trend of surface temperature on the building roof and walls was observed at the nighttime, this paper assumed the heat flux from all building/ground surfaces was the same and estimated the kinematic sensible heat flux (*H*) based on the maximum nighttime temperature difference between the surfaces and ambient air:

$$H = \frac{h(T_{surface} - T_{air})}{cp \cdot \rho} \qquad (8)$$

where *h* refers to the convective heat transfer coefficient, which is assumed to be 8 $W \cdot K^{-1} \cdot m^{-2}$ based on the numerical estimation in urban-like settings given by Awol et al. [75]; $T_{surface}$ and T_{air} refer to the surface and air temperature, respectively; and ρ refers to the density of dry air (1.225 $kg \cdot m^{-3}$).

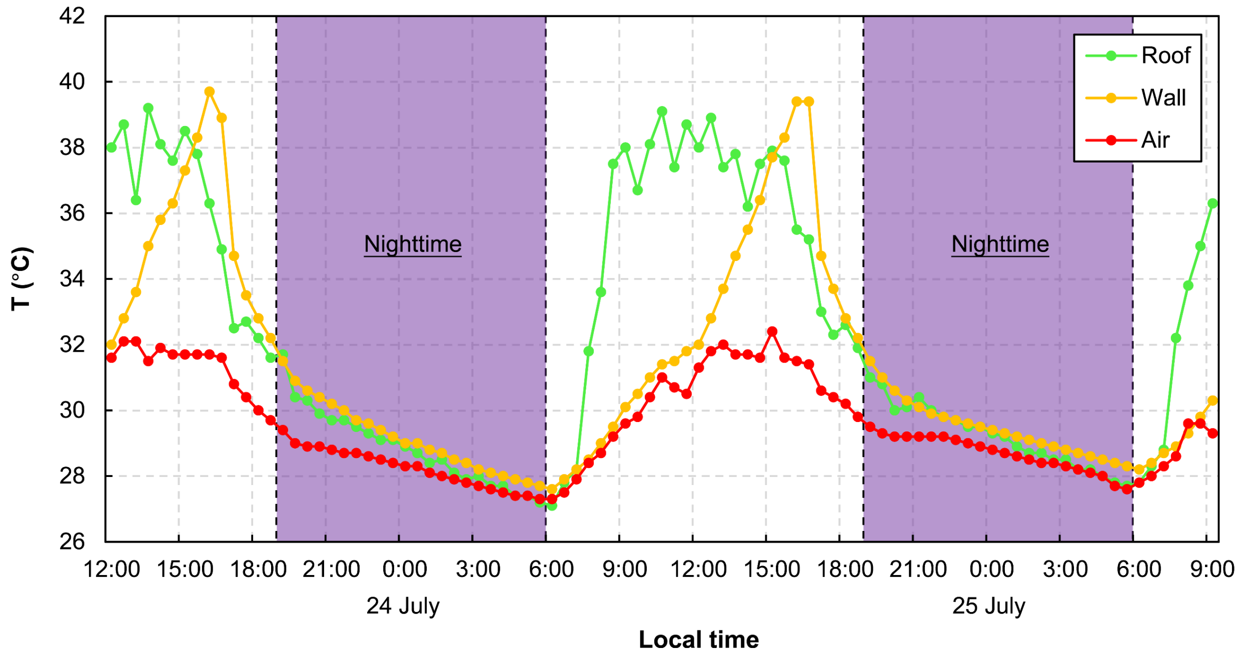

Fig. 6. Diurnal variations of surface (building roof and wall) and air temperature measured at Yam Pak building (Fig. 2) in Hong Kong University from 24 to 25 July in summer 2008 [74].

5. Results and Discussion

This section cross-compares the effects of three pairs of input parameters on CFD results as defined in Section 4.1: 1) conventionally-used wind profiles versus LiDAR wind profiles; 2) 24-hour-averaged wind profiles versus HN-averaged wind profiles; and 3) neutral thermal conditions versus unstable thermal conditions. In each pair of input parameters, the latter one is the benchmark-setting which specifies extreme hot weather conditions in HNs when reproducing inlet wind profiles and site thermal conditions. Sections 5.1 and 5.2 qualitatively and quantitatively analyze the pedestrian-level and upper-level wind speed, respectively. Section 5.3 further analyzes the pedestrian-level wind velocity ratio (as defined in Section 5.3).

5.1. Deviations of wind speed at the pedestrian level

5.1.1. Qualitative analysis

The pedestrian-level wind speed contours, simulated by CFD with different input parameters, are plotted in Figs. 7 and 8. The benchmark scenarios, i.e. LiDAR(HN)-U-I/II, in both the overall and extreme situations, are used to evaluate the other scenarios. Overall, the inlet wind profiles and site thermal conditions without specifying extreme hot weather conditions cause significant deviations on the assessment of pedestrian-level wind speed in HNs. Particularly, these deviations are more obvious in the extreme situation, which focuses on HNs in prolonged extreme heat.

Conventionally-used wind profiles versus LiDAR wind profiles (benchmark): Based on the benchmark scenarios with LiDAR observation, the conventionally-used (PL) wind profiles, i.e. PL(24H)-B-I/II, lead to significant overestimations of pedestrian-level wind speed in HNs. The overestimations can be explained by two reasons. Firstly, the power law formula itself has deficiencies that it cannot explicitly describe the shapes of wind profiles which are highly modified by urban heterogeneities and buoyancy effects [76, 77]. Secondly, the mesoscale meteorological modeling dataset (i.e. site wind availability data), which provides reference wind speed to the PL wind profiles [28], wrongly represent U_∞ in HNs. In this paper, the mesoscale meteorological model underestimates U_∞ in HNs in the overall situation (i.e. summer), and overestimates U_∞ in HNs in the extreme situation (i.e. prolonged extreme heat) as revealed in Fig. 4.

24-hour-averaged wind profiles versus HN-averaged wind profiles (benchmark): Overestimations of pedestrian-level wind speed in HNs are also induced by the 24-hour-averaged LiDAR wind profiles, i.e. LiDAR(24H)-U-I/II, although they are less obvious than those induced by the conventionally-used wind profiles. The deviations are mainly because the LiDAR observation in 24-hour-periods fails to specify the buoyancy effects in HNs, which can significantly modify the shapes of the upwind wind profiles (Fig. 4). In the extreme situation, the deviation is also caused by the overestimation of the advection in HNs in prolonged extreme heat by the 24-hour-averaged LiDAR data, as explained in Section 3.3.

Neutral thermal conditions versus unstable thermal conditions (benchmark): The neutral thermal conditions, i.e. LiDAR(HN)-N-I/II, which ignore buoyancy effects at the test site, cause underestimations of pedestrian-level wind speed in HNs. This result agrees with a previous study [59], which revealed a considerable enhancement on pedestrian-level wind speed by the buoyancy effects from high-density urban morphologies in nighttime calm conditions.

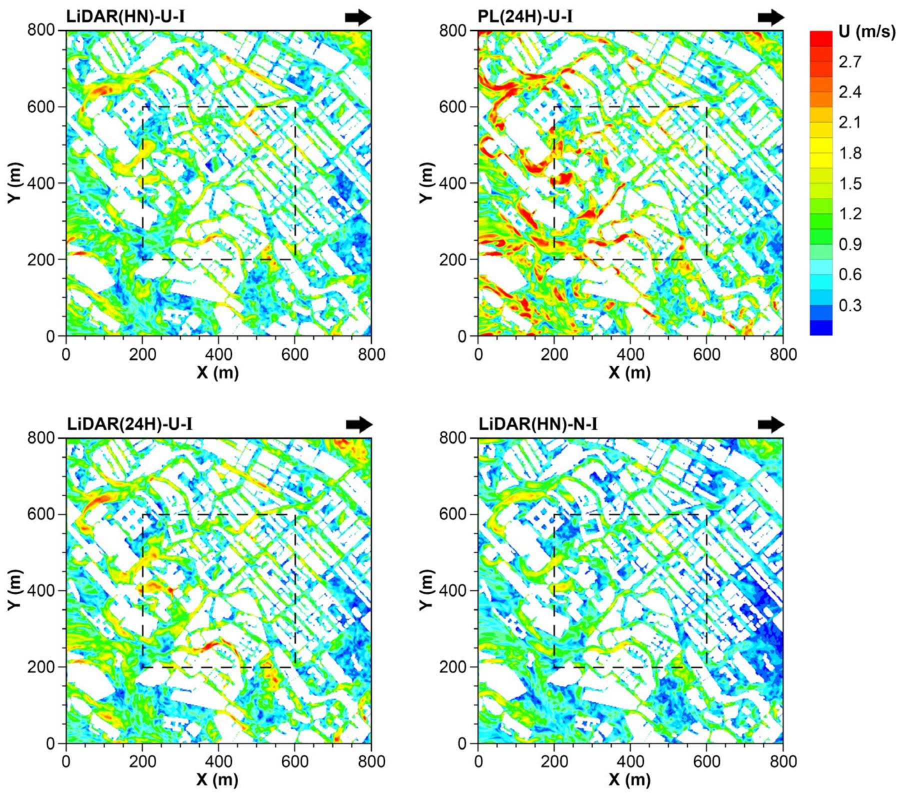

Fig. 7. Pedestrian-level distributions (Z = 2 m) of wind speed (*U*) with different inlet wind profiles and site thermal conditions in overall situation: hot nights (HNs) in summer.

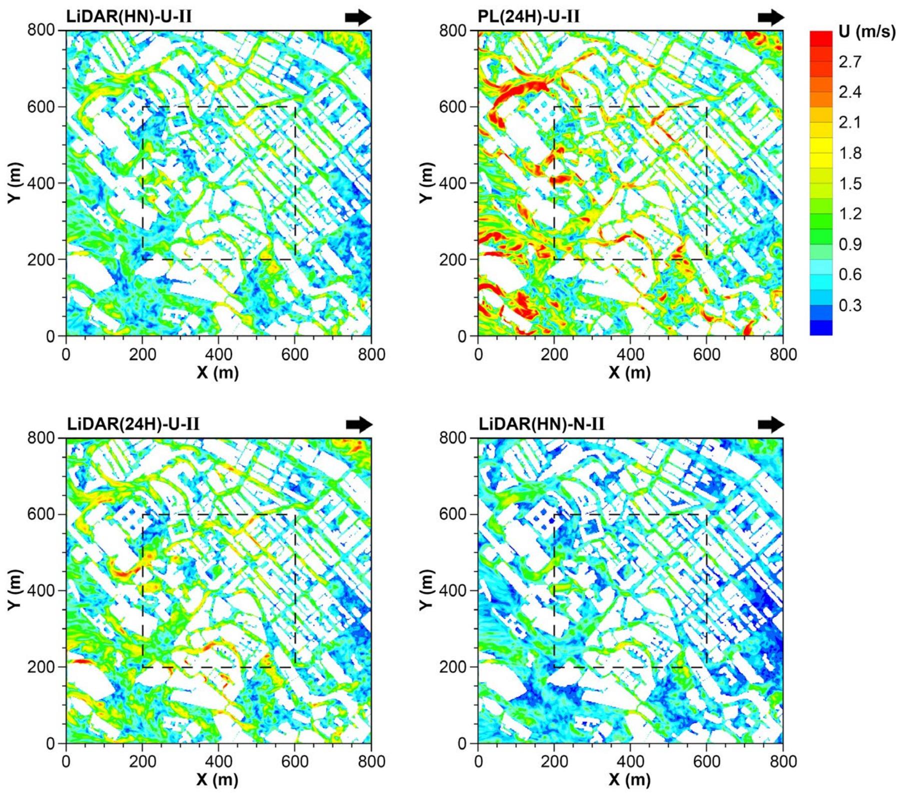

Fig. 8. Pedestrian-level distributions (Z = 2 m) of wind speed (*U*) with different inlet wind profiles and site thermal conditions in extreme situation: hot nights (HNs) in prolonged extreme heat.

5.1.2. Quantitative analysis

More than the qualitative analysis, we used two indicators, the percentage deviation of wind speed (PD_U) and percentage deviation of wind speed frequency (PD_F), to quantify the deviations on urban ventilation assessment caused by the inlet wind profiles and site thermal conditions which are lack of consideration of nighttime extreme heat. PD_U and PD_F are calculated as:

$$PD_U = \frac{U_{Evaluation} - U_{Benchmark}}{U_{Benchmark}} \times 100\% \qquad (9)$$

$$PD_F = \frac{F_{Evaluation} - F_{Benchmark}}{F_{Benchmark}} \times 100\% \qquad (10)$$

where $U_{Evaluation}$ and $U_{Benchmark}$ refer to the spatially-averaged wind speed from CFD simulations in the benchmark scenarios and the scenarios to be evaluated, respectively. Correspondingly, $F_{Evaluation}$ and $F_{Benchmark}$ refer to the frequency of the simulated wind speed in the benchmark scenarios and the scenarios to be evaluated, respectively. The calculation of the two indicators was conducted at the central target area of 400 m (*X*) × 400 m (*Y*) of the test site (Figs. 7 and 8).

The results of PD_U at the pedestrian level are shown in Fig. 9. The largest deviations are caused by the conventionally-used (PL) wind profiles, i.e. PL(24H)-U-I/II, which overestimate over 30% and 45% of pedestrian-level wind speed in HNs in the overall (i.e. summer) and extreme (i.e. prolonged extreme heat) situations, respectively. These deviations (Part B) are larger than those in Part A [34], where we have indicated that the PL method overestimates the pedestrian-level wind speed by around 25% at the same test site in summer. The larger deviations in the current paper suggest that the conventional methods to reproduce wind profiles can cause further inaccuracy for assessing pedestrian-level wind in HNs where the buoyancy effects are specified. Besides, smaller but still significant deviations are seen when using either the 24-hour-averaged LiDAR wind profiles, i.e. LiDAR(24H)-U-I/II, or the neutral thermal conditions, i.e. LiDAR(HN)-N-I/II. They either overestimate or underestimate pedestrian-level wind speed by over 20%. This result suggests that the improper use of the LiDAR observational data can also cause intolerable mistakes in pedestrian-level wind assessment outputs.

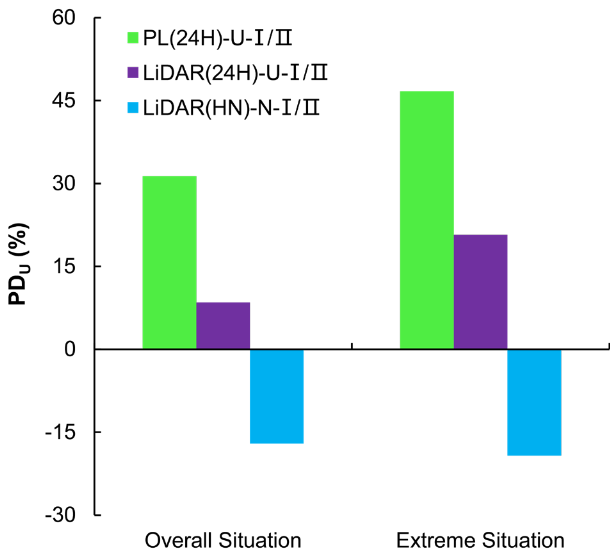

Fig. 9. Percentage deviation of pedestrian-level wind speed (PD_U) in hot nights (HNs) of different scenarios in overall situation: HNs in summer; and extreme situation: HNs in prolonged extreme heat.

Furthermore, the results of PD_F are given by categorizing the simulated pedestrian-level wind speed into three ranges: comfort (> 1.3 m/s), medium (0.3 – 1.3 m/s), and poor (≤ 0.3 m/s). This criterion [78] was established to evaluate the influence of wind speed on outdoor thermal comfort based on the surveys conducted by Cheng et al. [79] and Ng et al. [80] in Hong Kong. As shown in Fig. 10, based on the simulations results, obvious deviations are seen at both the comfort and poor zones. Among the scenarios to be evaluated, the conventionally-used (PL) wind profiles cause the largest deviations of almost 200%, and the deviations caused by the 24-hour-averaged LiDAR wind profiles and neutral thermal conditions are over 70%. Particularly, the deviations caused by the PL wind profiles in the current paper (Part B) are double of those in Part A [34] (i.e. deviations > 100%). These large deviations suggest the importance of explicit consideration of buoyancy effects in pedestrian-level wind assessment for addressing outdoor thermal comfort.

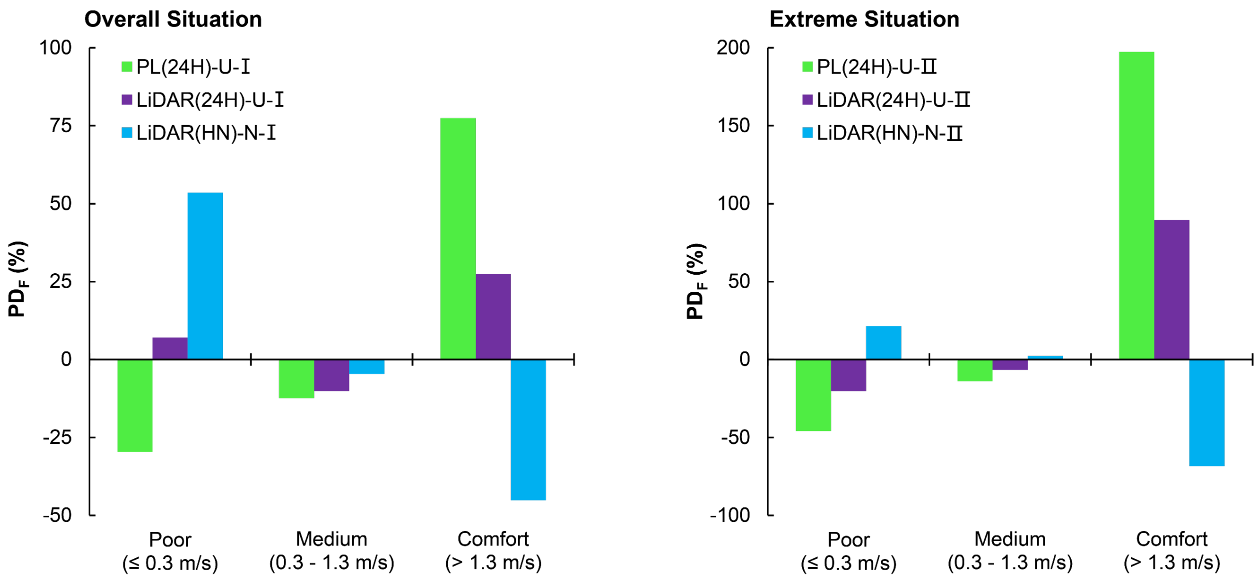

Fig. 10. Percentage deviation of pedestrian-level wind speed frequency (PD_F) in hot nights (HNs) at three ranges of wind comfort [78] of different scenarios in an overall situation: HNs in summer; and extreme situation: HNs in prolonged extreme heat.

5.2. Deviations of wind speed at the upper level

5.2.1. Qualitative analysis

The stream-wise (along X dimension) wind speed distributions in the vertical dimension are shown in Figs. 11 and 12. The analysis mainly focuses on the upper levels till around 200 m, covering the urban canopy layer in Hong Kong (0 – 60 m [81]), and the highest buildings at the test site (around 180 m). Based on the benchmark scenarios, i.e. LiDAR(HN)-B-I/II, in both the overall and extreme situations, the deviations caused by the inlet wind profiles or site thermal conditions without specifying nighttime extreme hot weather conditions are as follows:

Conventionally-used wind profiles versus LiDAR wind profiles (benchmark): The conventional (PL) method, i.e. PL(24H)-U-I/II, largely overestimates the mean flow within and just above the urban canopy layer in HNs. Consequently, the conventional method causes deviations when predicting both the mechanical and buoyancy effects on turbulent motions from urban morphologies since these effects are sensitive to the incoming flow at high-density urban areas [61]. Particularly, in the extreme situation where prolonged extreme heat occurs, the conventional method causes even larger deviations of the mean flow and turbulent motions due to the stronger buoyancy effects and weaker incoming wind conditions.

24-hour-averaged wind profiles versus HN-averaged wind profiles (benchmark): The 24-hour-averaged LiDAR wind profiles, LiDAR(24H)-U-I/II, which do not specify the effects of thermal buoyancy and advection at the upwind in HNs, also overestimate the mean flow and turbulent motions in the vertical wind assessment. Similar as the PL wind profiles, the 24-hour-averaged LiDAR wind profiles cause stronger and more intense vertical mixing within and just above the urban canopy layer.

Neutral thermal conditions versus unstable thermal conditions (benchmark): the neutral thermal conditions, i.e. LiDAR(HN)-N-I/II, which do not take into account the buoyancy effects at the site in HNs, lead to less vertical mixing within the urban canopy layer and more laminar flow structure above the layer than the observation by LiDAR. The result reveals the deficiency of the neutral thermal conditions on reproducing the unstably-stratified vertical wind distributions under extreme hot weather conditions at a high-density urban site. It is consistent with some previous findings on urban boundary layer flow [69, 82].

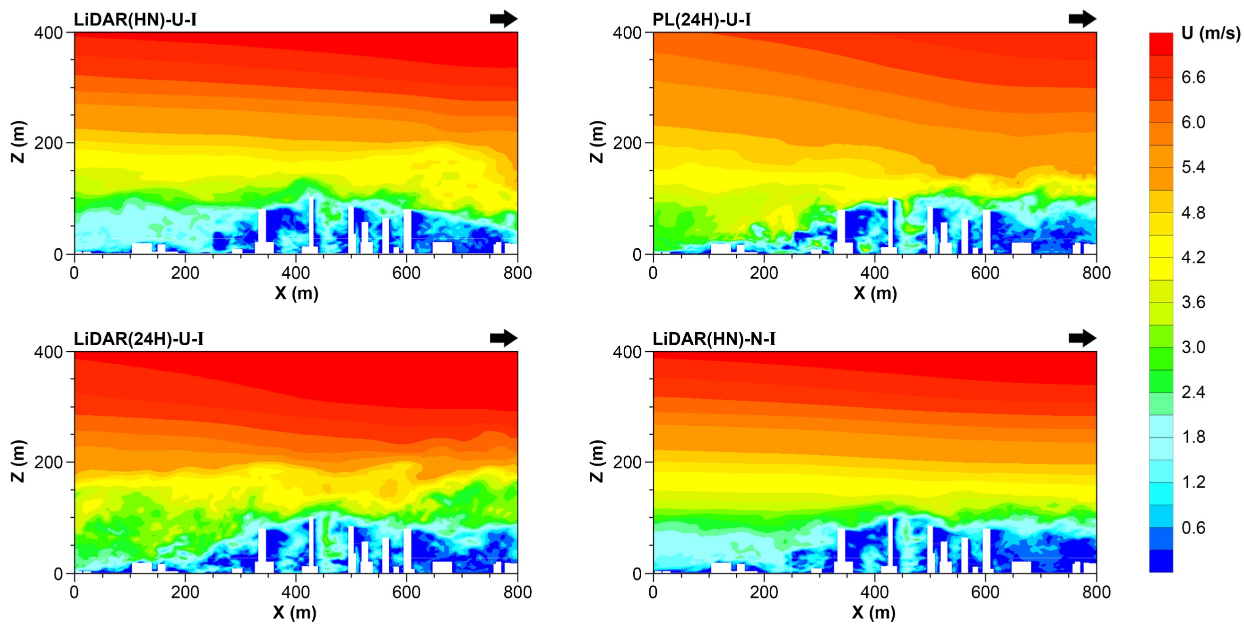

Fig. 11. Vertical distributions (Y = 400 m) of wind speed (*U*) along prevailing southwest wind direction with different inlet wind profiles and site thermal conditions in overall situation: hot nights (HNs) in summer.

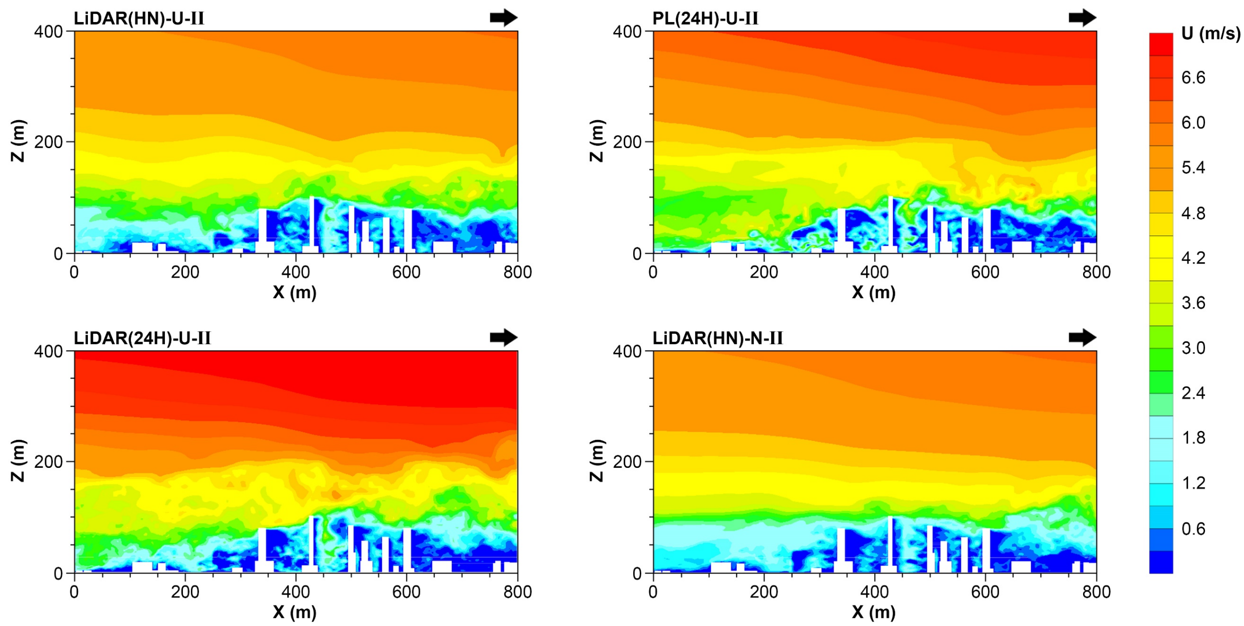

Fig. 12. Vertical distributions (Y = 400 m) of wind speed (*U*) along prevailing southwest wind direction with different inlet wind profiles and site thermal conditions in extreme situation: hot nights (HNs) in prolonged extreme heat.

5.2.2. Quantitative analysis

The simulated wind speed at the upper levels (i.e., 0 – 240 m) above the target area are quantitatively compared by PD_U, as depicted in Fig. 13. Similar as the results at the pedestrian level, the inlet wind profiles or site thermal conditions that do not specify extreme hot weather conditions lead to more obvious deviations in the extreme situation (i.e. prolonged extreme heat) than the overall situation (i.e. summer) in HNs at the upper levels. The largest deviations are seen within the urban canopy layer, where the scenarios based on the conventional (PL) method, i.e. PL(24H)-U-I/II, cause the deviations of over 45%, and the scenarios based on LiDAR observation, i.e. LiDAR(24H)-U-I/II and LiDAR(HN)-N-I/II, cause the deviations of over 25%. These large deviations may cause misleading results in upper-level wind assessment inside street canyons, especially the deep ones, where the heat is easily trapped at nighttime [67]. They may also mislead the other assessment associated with the outdoor wind field, such as the assessment of outdoor pollutant dispersion and indoor natural ventilation.

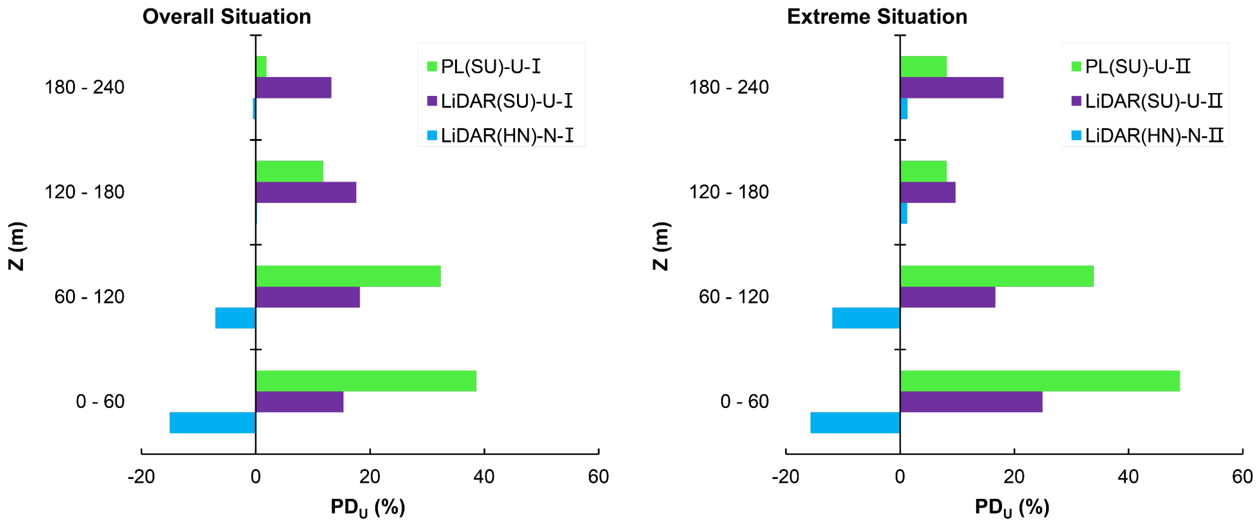

Fig. 13. Percentage deviation of wind speed (PD_U) at upper levels (0 – 240 m) in hot nights (HNs) of different scenarios in overall situation: HNs in summer; and extreme situation: HNs in prolonged extreme heat.

5.3. Deviations of wind velocity ratio at the pedestrian level

In addition to the analysis of wind speed, we converted wind speed into wind velocity ratio (*VR*) to indicate the wind availability at different heights of the test site by the following equation:

$$VR = \frac{U}{U_\infty} \qquad (11)$$

where U refers to the simulated wind speed at an evaluation height; and U_∞ refers to the upwind wind speed at the height of 500 m (Fig. 4). The simulated vertical *VR* profiles of different scenarios over the target area are shown in Fig. 14. Compared with wind speed, *VR* more clearly describes the shapes of wind profiles modified by both of the mechanical and thermal effects since it excludes the impacts of the incoming wind scale (as indicated by U_∞). Thus, *VR* is currently used as the indicator in AVA as required by the technical circular [28].

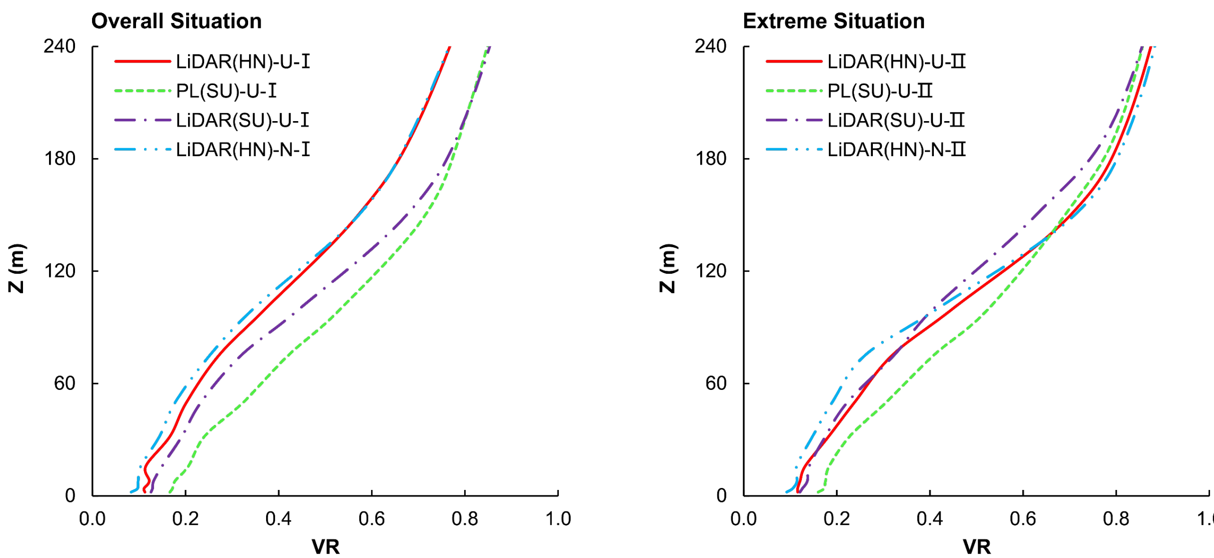

Fig. 14. Simulated vertical wind velocity ratio (*VR*) profiles at upper levels (0 – 240 m) in hot nights (HNs) of different scenarios in overall situation: HNs in summer; and extreme situation: HNs in prolonged extreme heat.

Based on the simulated *VR*, we used an indicator, the percentage deviation of wind velocity ratio (PD_{VR}), to quantify the deviations on pedestrian-level wind assessment caused by the inlet wind profiles and site thermal conditions to be evaluated. PD_{VR} is calculated as:

$$PD_{VR} = \frac{VR_{Evaluation} - VR_{Benchmark}}{VR_{Benchmark}} \times 100\% \qquad (12)$$

where $VR_{Evaluation}$ and $VR_{Benchmark}$ refer to the *VR* at the pedestrian level from CFD in the benchmark scenarios (i.e. LiDAR(HN)-U-I/II) and the scenarios to be evaluated, respectively.

The distributions of PD_{VR} of different scenarios to be evaluated are depicted in Fig. 15. The largest deviations are seen in the scenarios using the conventional (PL) wind profiles (i.e. PL(24H)-U-I/II). These deviations are more obvious distributed at the zones with larger open spaces. Furthermore, the spatially-averaged PD_{VR} caused by different input parameters are summarized in Fig. 16: over 45% by the PL wind profiles (i.e. PL(24H)-U-I/II); around 10% by the 24-hour-averaged LiDAR wind profiles (i.e. LiDAR(24H)-U-I/II); and over 15% by the neutral thermal conditions (i.e. LiDAR(HN)-N-I/II). Different from the results of PD_U at the pedestrian level in Section 4.1.2, which indicate larger deviations in the extreme situation (i.e. prolonged extreme heat) than the overall situation (i.e. summer), an opposite trend is seen in the results of PD_{VR}. Particularly, in the extreme situation, PD_U caused by the 24-hour-averaged LiDAR wind profile is over 20% (Fig. 9), while the results of PD_{VR} turn out to be negligible. On one hand, the larger deviation on pedestrian-level wind speed is attributed to the different U_∞ between 24-hour-periods and HNs in prolonged extreme heat, as confirmed in Fig. 4. On the other hand, the smaller deviation on pedestrian-level *VR* suggests that the buoyancy effects of modifying the shapes of wind profiles are comparable between 24-hour-periods and HNs in prolonged extreme heat, as confirmed in Fig. 14. Despite that the 24-hour-averaged LiDAR wind profile only causes small PD_{VR}, it may still cause a large deviation on the wind speed field in HNs, due to the inexplicit coupling effects between vertical mixing induced by thermal buoyancy and horizontal flow induced by advection.

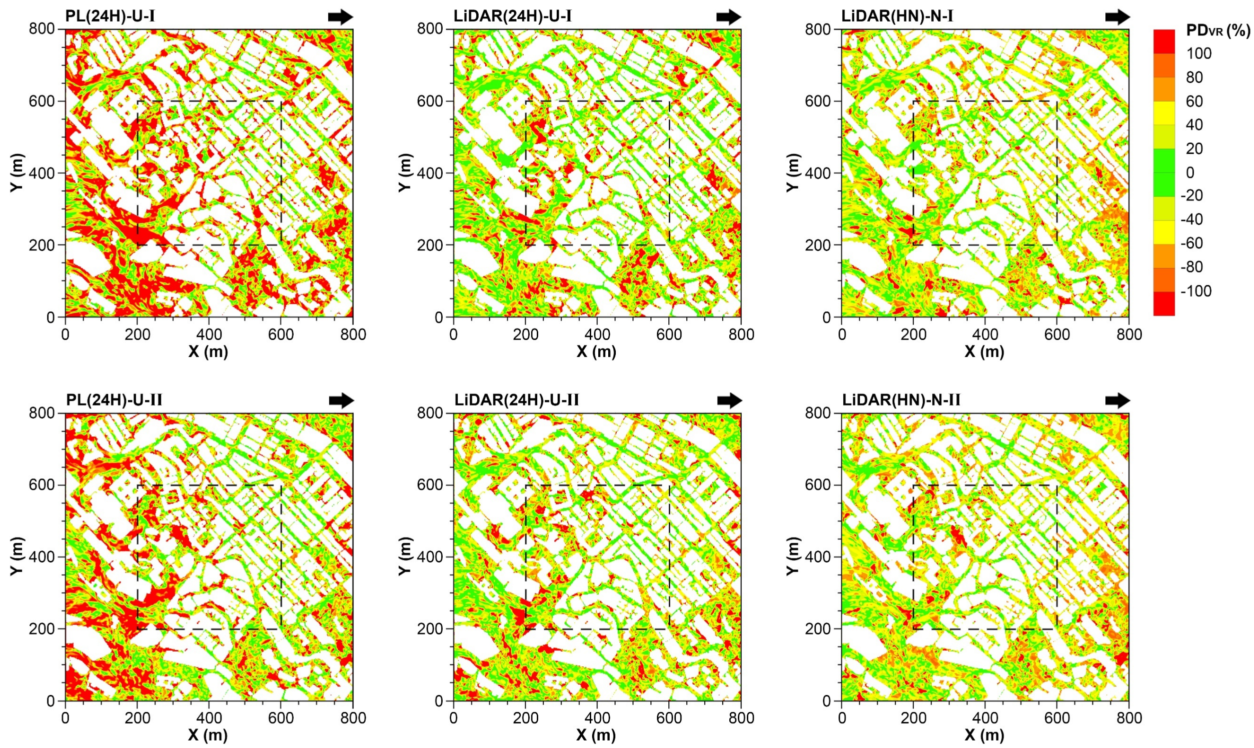

Fig. 15. Pedestrian-level distributions (Z = 2 m) of percentage deviation of wind velocity ratio (PD_{VR}) in hot nights (HNs) of different scenarios in overall situation: HNs in summer; and extreme situation: HNs in prolonged extreme heat.

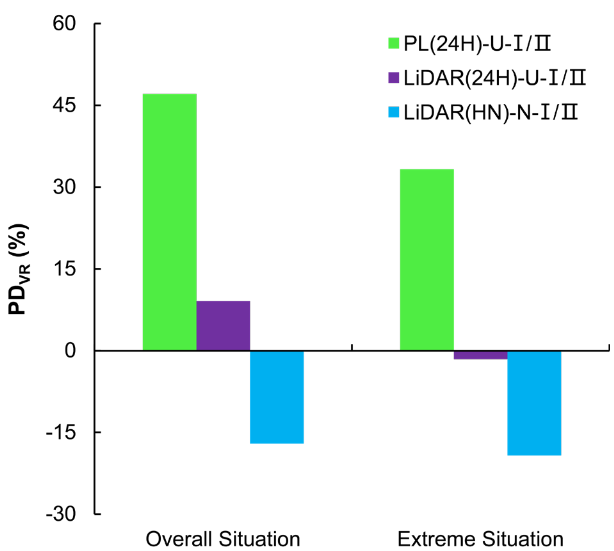

Fig. 16. Percentage deviation of pedestrian-level wind velocity ratio (PD_{VR}) in hot nights (HNs) of different scenarios in overall situation: HNs in summer; and extreme situation: HNs in prolonged extreme heat.

6. Final Discussion and Conclusion

This study uses LiDAR observation to cross-compare the HN-averaged and 24-hour-averaged vertical wind speed profiles in summer at a typical high-density urban area in Hong Kong. The observation in HNs involves two situations: 1) overall situation (i.e. HNs in summer); and 2) extreme situation (i.e. HNs in prolonged extreme heat). Based on the observational data, CFD simulations with LES model are conducted to evaluate the deviations of urban ventilation assessment caused by the lack of consideration of extreme hot weather conditions in HNs. Three pairs of input parameters are compared in CFD: 1) conventionally-used power law (PL) wind profile versus LiDAR wind profiles; 2) 24-hour-averaged wind profile versus HN-averaged wind profiles; and 3) neutral thermal conditions versus unstable thermal conditions. Major findings are summarized and discussed on two aspects. Firstly, this study establishes a better understanding of wind conditions in high-density cities in nighttime extreme heat:

- Based on LiDAR observation, this study reveals weaker urban wind conditions in HNs than 24-hour-periods in summer (Fig. 4). It means that urban dwellers suffer from not only higher-than-normal air temperature but also lower-than-normal wind speed in nighttime extreme heat.
- Particularly, the weakest pedestrian-level urban wind environment is found in HNs during prolonged extreme heat, leading to deteriorating heat-related health issues in Hong Kong [83].
- The current findings call for more attentions to the wind conditions in high-density cities in nighttime extreme heat given that they are weaker than the averaged wind conditions in summer, and crucial for releasing heat-stress for human thermal comfort and public health.

Secondly, this study provides recommendations to improve the current methodology in AVA to address the impacts of nighttime extreme heat on urban ventilation:

- The conventional methods, e.g. PL (power law) method, to reproduce vertical wind speed profiles causes significant deviations on pedestrian-level wind speed (> 45%) and wind speed frequency (> 200%) in HNs (Figs. 9 and 10). These deviations are even larger than those revealed in Part A [34], where the PL method was used to predict pedestrian-level wind conditions in summer (wind speed (> 25%); and wind speed frequency (> 100%)).
- Alternatively, the LiDAR observation to reproduce vertical wind speed profiles is more accurate. However, it is recommended to address the influence of specific thermal conditions on the flow at both the upwind (via measurements of wind profiles) and the test site (via simulations of thermal buoyancy) when assessing the pedestrian-level wind in HNs. Otherwise, considerable deviations are caused (wind speed (> 20%); and wind speed frequency (> 70%)) (Figs. 9 and 10).
- For AVA, the conventional methods, e.g. PL method, are not recommended for assessing urban wind environments in extremely high-temperature and weak-wind conditions at nighttime due to the significant deviations on pedestrian-level *VR* (> 45%) (Fig. 16). More importantly, the conventional method hardly explicitly reproduces the unstable vertical flow structure induced by the coupling effects between thermal buoyancy and advection (Figs. 11 and 12), due to the deviations of wind speed within and above the urban

canopy layer. As such, the LiDAR observational data, preferably considering the extreme heat, is required to optimize the current site wind availability data for tackling the periods when the wind is most needed for heat-stress relief.

The different heat-wind relationships revealed in this study imply the needs of categorical understanding on the wind conditions under diverse hot periods. It is particularly important to better understand and assess the wind behaviors in high-density cities in nighttime extreme heat in summer given that they become excessive and are highly associated with public health. A better understanding and assessment of the "new normal" wind conditions are crucial for developing wind-adaptive urban planning/design strategies for a healthier and more comfortable living environment.

7. Limitations and Future Works

This paper only investigates the extreme heat at nighttime, while a subsequent investigation will be needed to tackle the situations at the daytime, where wind conditions are expected to be more unstable due to the stronger buoyancy effects induced by solar radiation. In addition, the paper only involves a typical urban site, while more urban areas and building densities should be studied in the future in order to diversify the buoyancy effects on urban ventilation.

Declaration of competing interest

The authors declare that they have no known competing financial interests or personal relationships that could have appeared to influence the work reported in this paper.

Acknowledgement

The study is partially supported by the CUHK Research Sustainability of Major RGC Funding Scheme (CRF-2016/17-C4020-16G-3133195). It is partially supported by the Environmental Protection Department (EPD) project named 'monitoring vertical wind velocity and turbulent intensity profiles in the high-density urban boundary layer in Hong Kong (20-04955)'. Thanks are due to Prof. Jimmy Chi Hung Fung's team in Hong Kong University of Science and Technology and Prof. Yuguo Li's team in Hong Kong University for maintaining the wind LiDAR. Thanks are also due to Hong Kong Observatory (HKO) for providing air temperature data in summer 2020.

Appendix A. LiDAR validation

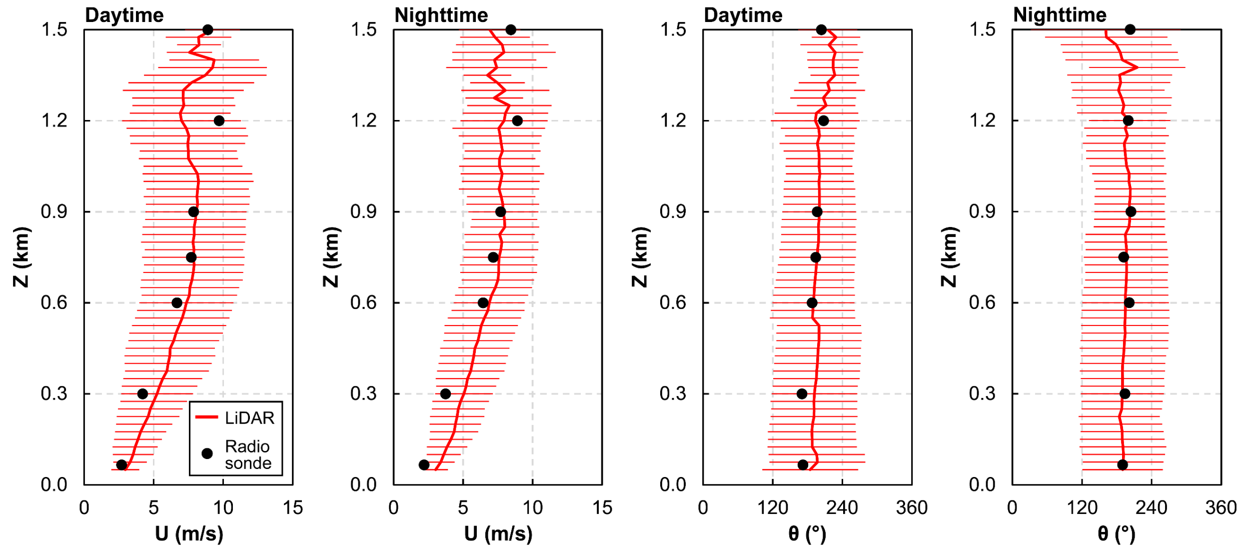

Fig. 17. Comparison of nighttime/daytime vertical profiles of horizontal wind speed (*U*) and direction (θ) (i.e., mean and standard deviations) measured by radiosondes and a wind LiDAR at the King's Park meteorological station at 8 am and 8 pm daily [63] in a period of two weeks, where the overall R^2 reaches 0.88 and 0.82 for *U* and θ, respectively. The validation results confirm consistently high reliability of the LiDAR observational data at both the daytime and nighttime.

Appendix B. LES validation

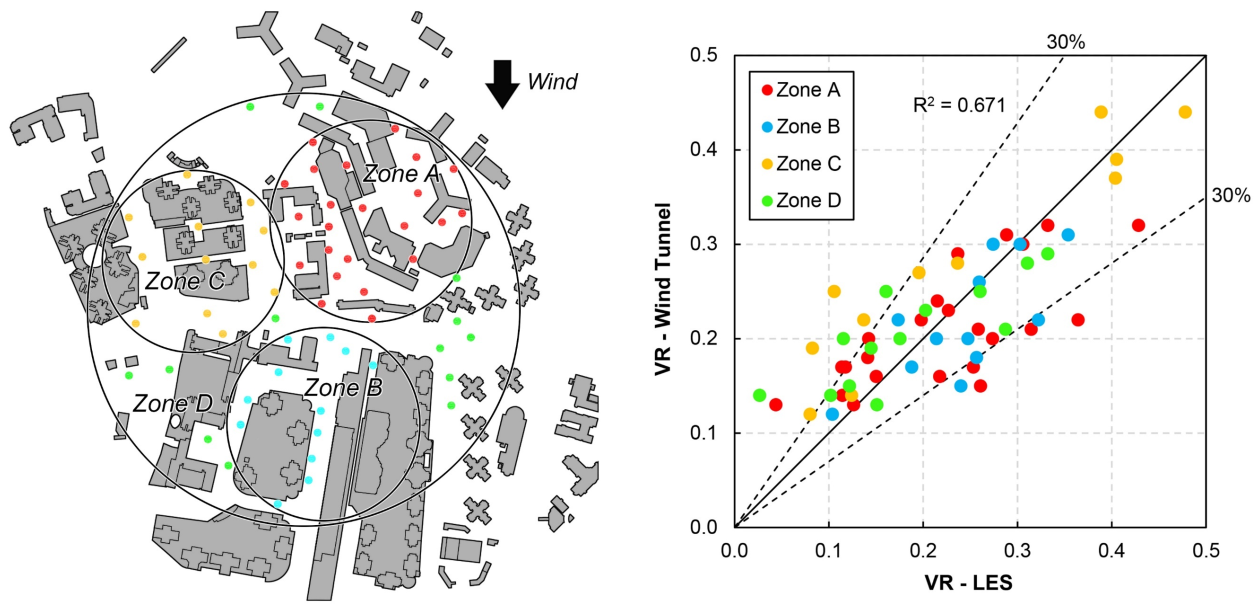

Fig. 18. Comparison of pedestrian-level wind velocity ratio (*VR*) obtained by low-speed wind tunnel experiments [84] and the current LES model at a high-density urban site in Sai Kung, Hong Kong under the northwest wind direction. The validation results based on 60 test points show the overall R^2 reaching around 0.7 and the root mean square error reaching around 0.06, which are in line with previous validation results in PALM with high-density urban settings in both neutral [82, 85] and thermal [82, 86] stratifications. More detailed validation results have been reported in Part A [34].

Reference

1. Blocken, B., W. Janssen, and T. van Hooff, *CFD simulation for pedestrian wind comfort and wind safety in urban areas: General decision framework and case study for the Eindhoven University campus.* Environmental Modelling & Software, 2012. **30**: p. 15-34.
2. Höppe, P., *The physiological equivalent temperature–a universal index for the biometeorological assessment of the thermal environment.* International Journal of Biometeorology, 1999. **43**(2): p. 71-75.
3. Cheng, V., E. Ng, C. Chan, and B. Givoni, *Outdoor thermal comfort study in a sub-tropical climate: a longitudinal study based in Hong Kong.* International Journal of Biometeorology, 2012. **56**(1): p. 43-56.
4. He, Y., A. Tablada, and N.H. Wong, *Effects of non-uniform and orthogonal breezeway networks on pedestrian ventilation in Singapore's high-density urban environments.* Urban Climate, 2018. **24**: p. 460-484.
5. He, Y., A. Tablada, and N.H. Wong, *A parametric study of angular road patterns on pedestrian ventilation in high-density urban areas.* Building and Environment, 2019. **151**: p. 251-267.
6. BCA, *Ventilation simulation methodology and requirements, BCA Green Mark certification standard for new buildings*. 2012, Building and Construction Authority (BCA): Singapore.
7. MOE, *Outline of the policy framework to reduce urban heat island effects*. 2004, Ministry of the Environment (MOE): Japan.
8. Ng, E., *Policies and technical guidelines for urban planning of high-density cities–air ventilation assessment (AVA) of Hong Kong.* Building and Environment, 2009. **44**(7): p. 1478-1488.
9. IPCC, *Summary for Policymakers. In: Climate Change 2021: The Physical Science Basis. Contribution of Working Group I to the Sixth Assessment Report of the Intergovernmental Panel on Climate Change*. 2021, Cambridge University Press.
10. García-Herrera, R., J. Díaz, R.M. Trigo, J. Luterbacher, and E.M. Fischer, *A review of the European summer heat wave of 2003.* Critical Reviews in Environmental Science and Technology, 2010. **40**(4): p. 267-306.
11. Heaviside, C., S. Vardoulakis, and X.-M. Cai, *Attribution of mortality to the urban heat island during heatwaves in the West Midlands, UK.* Environmental Health, 2016. **15**(1): p. 49-59.
12. Nitschke, M., G.R. Tucker, A.L. Hansen, S. Williams, Y. Zhang, and P. Bi, *Impact of two recent extreme heat episodes on morbidity and mortality in Adelaide, South Australia: a case-series analysis.* Environmental Health, 2011. **10**(1): p. 1-9.
13. Robinson, P.J., *On the definition of a heat wave.* Journal of Applied Meteorology and Climatology, 2001. **40**(4): p. 762-775.
14. Smith, T.T., B.F. Zaitchik, and J.M. Gohlke, *Heat waves in the United States: definitions, patterns and trends.* Climatic Change, 2013. **118**(3): p. 811-825.
15. Lemonsu, A., V. Viguie, M. Daniel, and V. Masson, *Vulnerability to heat waves: Impact of urban expansion scenarios on urban heat island and heat stress in Paris (France).* Urban Climate, 2015. **14**: p. 586-605.
16. Meehl, G.A. and C. Tebaldi, *More intense, more frequent, and longer lasting heat waves in the 21st century.* Science, 2004. **305**(5686): p. 994-997.
17. Tan, J., Y. Zheng, X. Tang, C. Guo, L. Li, G. Song, X. Zhen, D. Yuan, A.J. Kalkstein, and F. Li, *The urban heat island and its impact on heat waves and human health in Shanghai.* International Journal of Biometeorology, 2010. **54**(1): p. 75-84.
18. Barlow, J.F., *Progress in observing and modelling the urban boundary layer.* Urban Climate, 2014. **10**: p. 216-240.

19. HKO. *Climatological database*. 2020 [cited 2021 July 15]; Available from: https://www.hko.gov.hk/en/cis/climat.htm.
20. HKO. *Number of hot nights observed at the Hong Kong Observatory since 1884*. 2020 [cited 2021 July 15]; Available from: https://www.hko.gov.hk/en/cis/statistic/hngtday_statistic.htm.
21. HKO. *Number of very hot days observed at the Hong Kong Observatory since 1884*. 2020 [cited 2021 July 15]; Available from: https://www.hko.gov.hk/en/cis/statistic/vhotday_statistic.htm.
22. HKO. *Climate projections for Hong Kong*. 2019 [cited 2021 8 Feb]; Available from: https://www.hko.gov.hk/en/climate_change/proj_hk_temp.htm.
23. Ren, C., K. Wang, Y. Shi, Y.T. Kwok, T. Morakinyo, T.-c. Lee, and Y. Li, *Investigating the urban heat and cool island effects during extreme heat events in high density cities A case study of Hong Kong from 2000-2018.* International Journal of Climatology, 2021.
24. Goggins, W.B., E.Y. Chan, E. Ng, C. Ren, and L. Chen, *Effect modification of the association between short-term meteorological factors and mortality by urban heat islands in Hong Kong.* PloS One, 2012. **7**(6): p. e38551.
25. Ho, H.C., K.K.-L. Lau, C. Ren, and E. Ng, *Characterizing prolonged heat effects on mortality in a sub-tropical high-density city, Hong Kong.* International Journal of Biometeorology, 2017. **61**(11): p. 1935-1944.
26. Wang, D., K.K.-L. Lau, C. Ren, W.B.I. Goggins, Y. Shi, H.C. Ho, T.-C. Lee, L.-S. Lee, J. Woo, and E. Ng, *The impact of extremely hot weather events on all-cause mortality in a highly urbanized and densely populated subtropical city: A 10-year time-series study (2006–2015).* Science of The Total Environment, 2019. **690**: p. 923-931.
27. Shi, Y., C. Ren, M. Cai, K.K.-L. Lau, T.-C. Lee, and W.-K. Wong, *Assessing spatial variability of extreme hot weather conditions in Hong Kong: A land use regression approach.* Environmental Research, 2019. **171**: p. 403-415.
28. HPLB and ETWB, *Technical circular no. 1/06: Air ventilation assessments*. 2006, Housing, Planning and Lands Bureau (HPLB) and Environment, Transport and Works Bureau(ETWB), Hong Kong SAR government Hong Kong.
29. NUS. *Urban climatic mapping studies for Singapore*. 2021 [cited 2021.
30. RAIA. *The Lord Mayor's Brisbane buildings that breathes*. 2021 [cited 2021; Available from: https://www.architecture.com.au/archives/.
31. Ren, C., R. Yang, C. Cheng, P. Xing, X. Fang, S. Zhang, H. Wang, Y. Shi, X. Zhang, and Y.T. Kwok, *Creating breathing cities by adopting urban ventilation assessment and wind corridor plan–the implementation in Chinese cities.* Journal of Wind Engineering and Industrial Aerodynamics, 2018. **182**: p. 170-188.
32. Tieben, H., J. Chu, N. Soares, and E. Yiu. *Environmental Urban design and planning rules and their impact on street spaces in Hong Kong and Macau*. in *Proceedings of the 8th Conference International Forum on Urbanism, True Smart and Green City*. 2015. Citeseer.
33. PlanD. *Site wind availability data*. 2019 [cited 2021 July 15]; Available from: https://www.pland.gov.hk/pland_en/info_serv/site_wind/index.html.
34. He, Y., C. Yuan, C. Ren, and E. Ng, *Optimized urban ventilation assessment by better reproducing vertical wind profile in high-density cities – Part A: Comparisons between LiDAR and conventional methods.* Working paper, 2022.
35. Xoplaki, E., J.F. González-Rouco, J. Luterbacher, and H. Wanner, *Mediterranean summer air temperature variability and its connection to the large-scale atmospheric circulation and SSTs.* Climate Dynamics, 2003. **20**(7-8): p. 723-739.
36. Oke, T.R., *Boundary layer climates*. 2002: Routledge.

37. Rogers, C.D., A.J. Gallant, and N.J. Tapper, *Is the urban heat island exacerbated during heatwaves in southern Australian cities?* Theoretical and Applied Climatology, 2019. **137**(1): p. 441-457.
38. Sun, T., S. Kotthaus, D. Li, H.C. Ward, Z. Gao, G.-H. Ni, and C.S.B. Grimmond, *Attribution and mitigation of heat wave-induced urban heat storage change.* Environmental Research Letters, 2017. **12**(11): p. 114007.
39. Toparlar, Y., B. Blocken, P.v. Vos, G. Van Heijst, W. Janssen, T. van Hooff, H. Montazeri, and H. Timmermans, *CFD simulation and validation of urban microclimate: A case study for Bergpolder Zuid, Rotterdam.* Building and Environment, 2015. **83**: p. 79-90.
40. Gutiérrez, E., J.E. González, A. Martilli, R. Bornstein, and M. Arend, *Simulations of a heat-wave event in New York City using a multilayer urban parameterization.* Journal of Applied Meteorology and Climatology, 2015. **54**(2): p. 283-301.
41. Founda, D. and M. Santamouris, *Synergies between Urban Heat Island and Heat Waves in Athens (Greece), during an extremely hot summer (2012).* Scientific reports, 2017. **7**(1): p. 1-11.
42. Khan, H.S., R. Paolini, M. Santamouris, and P. Caccetta, *Exploring the synergies between urban overheating and heatwaves (HWs) in western Sydney.* Energies, 2020. **13**(2): p. 470.
43. Ramamurthy, P., J. Gonzalez, L. Ortiz, M. Arend, and F. Moshary, *Impact of heatwave on a megacity: an observational analysis of New York City during July 2016.* Environmental Research Letters, 2017. **12**(5): p. 054011.
44. Li, D., T. Sun, M. Liu, L. Wang, and Z. Gao, *Changes in wind speed under heat waves enhance urban heat islands in the Beijing metropolitan area.* Journal of Applied Meteorology and Climatology, 2016. **55**(11): p. 2369-2375.
45. Ngarambe, J., J. Nganyiyimana, I. Kim, M. Santamouris, and G.Y. Yun, *Synergies between urban heat island and heat waves in Seoul: The role of wind speed and land use characteristics.* Plos one, 2020. **15**(12): p. e0243571.
46. Zhang, C., Q. Wang, P.W. Chan, C. Ren, and Y. Li, *The effect of background wind on summertime daily maximum air temperature in Kowloon, Hong Kong.* Building and Environment, 2021: p. 108693.
47. Wu, Y., K. Zhao, J. Huang, M. Arend, B. Gross, and F. Moshary, *Observation of heat wave effects on the urban air quality and PBL in New York City area.* Atmospheric Environment, 2019. **218**: p. 117024.
48. He, Y., C. Ren, H.W.L. Mak, C. Lin, Z. Wang, J.C.H. Fung, Y. Li, A.K.H. Lau, and E. Ng, *Investigations of high-density urban boundary layer under summer prevailing wind conditions with Doppler LiDAR: A case study in Hong Kong.* Urban Climate, 2021. **38**: p. 100884.
49. Heaviside, C., X.M. Cai, and S. Vardoulakis, *The effects of horizontal advection on the urban heat island in Birmingham and the West Midlands, United Kingdom during a heatwave.* Quarterly Journal of the Royal Meteorological Society, 2015. **141**(689): p. 1429-1441.
50. Ortiz, L.E., J.E. Gonzalez, W. Wu, M. Schoonen, J. Tongue, and R. Bornstein, *New York City impacts on a regional heat wave.* Journal of Applied Meteorology and Climatology, 2018. **57**(4): p. 837-851.
51. Ramamurthy, P., D. Li, and E. Bou-Zeid, *High-resolution simulation of heatwave events in New York City.* Theoretical and Applied Climatology, 2017. **128**(1-2): p. 89-102.
52. Li, D. and E. Bou-Zeid, *Synergistic interactions between urban heat islands and heat waves: The impact in cities is larger than the sum of its parts.* Journal of Applied Meteorology and Climatology, 2013. **52**(9): p. 2051-2064.
53. Zhang, D.L., Y.X. Shou, and R.R. Dickerson, *Upstream urbanization exacerbates urban heat island effects.* Geophysical Research Letters, 2009. **36**(24).

54. Wang, Q., C. Zhang, C. Ren, J. Hang, and Y. Li, *Urban heat island circulations over the Beijing-Tianjin region under calm and fair conditions.* Building and Environment, 2020. **180**: p. 107063.
55. Wang, Q., J. Hang, Y. Fan, and Y. Li, *Urban plume characteristics under various wind speed, heat flux, and stratification conditions.* Atmospheric Environment, 2020. **239**: p. 117774.
56. Allegrini, J., V. Dorer, and J. Carmeliet, *Buoyant flows in street canyons: Validation of CFD simulations with wind tunnel measurements.* Building and Environment, 2014. **72**: p. 63-74.
57. Priyadarsini, R., W.N. Hien, and C.K.W. David, *Microclimatic modeling of the urban thermal environment of Singapore to mitigate urban heat island.* Solar energy, 2008. **82**(8): p. 727-745.
58. Yuan, C., A.S. Adelia, S. Mei, W. He, X.-X. Li, and L. Norford, *Mitigating intensity of urban heat island by better understanding on urban morphology and anthropogenic heat dispersion.* Building and Environment, 2020. **176**: p. 106876.
59. Mei, S.-J. and C. Yuan, *Three-dimensional simulation of building thermal plumes merging in calm conditions: Turbulence model evaluation and turbulence structure analysis.* Building and Environment, 2021. **203**: p. 108097.
60. Mei, S.-J. and C. Yuan, *Urban buoyancy-driven air flow and modelling method: A critical review.* Building and Environment, 2021: p. 108708.
61. Wang, W., X. Wang, and E. Ng, *The coupled effect of mechanical and thermal conditions on pedestrian-level ventilation in high-rise urban scenarios.* Building and Environment, 2021. **191**: p. 107586.
62. Antoniou, N., H. Montazeri, M. Neophytou, and B. Blocken, *CFD simulation of urban microclimate: Validation using high-resolution field measurements.* Science of the Total Environment, 2019. **695**: p. 133743.
63. HKO. *Upper-air weather measurements in Hong Kong*. 2019 [cited 2021 July 15]; Available from: https://www.hko.gov.hk/en/wservice/tsheet/uamet.htm.
64. Vaisal. *Wind energy WindCube*. 2021 [cited 2021 8 Feb]; Available from: https://www.vaisala.com/en/wind-lidars/wind-energy/windcube.
65. AIJ, *AIJ recommendations for loads on buildings*. 1996, Japan: Architectural Institute of Japan (AIJ).
66. PlanD, *Final report: Site wind availability system and web-based site wind availability database, Consultancy study on establishment of simulated site wind availability data for air ventilation assessments in Hong Kong*. 2013, Planning Department, Hong Kong SAR government (PlanD): Hong Kong.
67. Wong, N.H. and K.J. Steve, *Air temperature distribution and the influence of sky view factor in a green Singapore estate.* Journal of Urban Planning and Development, 2010. **136**(3): p. 261-272.
68. Maronga, B., S. Banzhaf, C. Burmeister, T. Esch, R. Forkel, D. Fröhlich, V. Fuka, K.F. Gehrke, J. Geletič, and S. Giersch, *Overview of the PALM model system 6.0.* Geoscientific Model Development, 2020. **13**(3): p. 1335-1372.
69. Gronemeier, T., S. Raasch, and E. Ng, *Effects of unstable stratification on ventilation in Hong Kong.* Atmosphere, 2017. **8**(9): p. 168.
70. Bentham, T. and R. Britter, *Spatially averaged flow within obstacle arrays.* Atmospheric Environment, 2003. **37**(15): p. 2037-2043.
71. Oke, T.R., *Initial guidance to obtain representative meteorological observations at urban sites, Instruments and observing methods, Report No. 81*. 2004, World Meteorological Organization.
72. Xie, Z.-T. and I.P. Castro, *Efficient generation of inflow conditions for large eddy simulation of street-scale flows.* Flow, Turbulence and Combustion, 2008. **81**(3): p. 449-470.
73. Rotach, M.W., S.E. Gryning, and C. Tassone, *A two-dimensional Lagrangian stochastic dispersion model for daytime conditions.* Quarterly Journal of the Royal Meteorological Society, 1996. **122**(530): p. 367-389.

74. Yang, L. and Y. Li, *City ventilation of Hong Kong at no-wind conditions.* Atmospheric Environment, 2009. **43**(19): p. 3111-3121.
75. Awol, A., G.T. Bitsuamlak, and F. Tariku, *Numerical estimation of the external convective heat transfer coefficient for buildings in an urban-like setting.* Building and Environment, 2020. **169**: p. 106557.
76. Drew, D.R., J.F. Barlow, and S.E. Lane, *Observations of wind speed profiles over Greater London, UK, using a Doppler lidar.* Journal of Wind Engineering and Industrial Aerodynamics, 2013. **121**: p. 98-105.
77. Kent, C.W., C.S.B. Grimmond, D. Gatey, and J.F. Barlow, *Assessing methods to extrapolate the vertical wind-speed profile from surface observations in a city centre during strong winds.* Journal of Wind Engineering and Industrial Aerodynamics, 2018. **173**: p. 100-111.
78. Yuan, C. and E. Ng, *Building porosity for better urban ventilation in high-density cities–A computational parametric study.* Building and Environment, 2012. **50**: p. 176-189.
79. Cheng, V. and E. Ng, *Thermal comfort in urban open spaces for Hong Kong.* Architectural Science Review, 2006. **49**(3): p. 236-242.
80. Ng, E., C. Chan, and V. Cheng, *Urban climatic map and standards for wind environment - feasibility study. Technical Input Report No.1: Methodologies and findings of user's wind comfort level survey*. 2008, Planning Department: Hong Kong.
81. Ng, E., C. Yuan, L. Chen, C. Ren, and J.C. Fung, *Improving the wind environment in high-density cities by understanding urban morphology and surface roughness: a study in Hong Kong.* Landscape and Urban Planning, 2011. **101**(1): p. 59-74.
82. Wang, W. and E. Ng, *Air ventilation assessment under unstable atmospheric stratification—A comparative study for Hong Kong.* Building and Environment, 2018. **130**: p. 1-13.
83. Wang, P., W.B. Goggins, Y. Shi, X. Zhang, C. Ren, and K.K.-L. Lau, *Long-term association between urban air ventilation and mortality in Hong Kong.* Environmental Research, 2021. **197**: p. 111000.
84. PlanD, *Working paper 2C: Wind tunnel benchmarking studies – batch II, Urban climatic map and standards for wind environment – feasibility study*. 2010, Planning Department, Hong Kong SAR government (PlanD): Hong Kong.
85. Gronemeier, T., K. Surm, F. Harms, B. Leitl, B. Maronga, and S. Raasch, *Validation of the dynamic core of the PALM model system 6.0 in urban environments: LES and wind-tunnel experiments.* Geosci Model Develop Discuss, 2020: p. 1-26.
86. Resler, J., K. Eben, J. Geletič, P. Krč, M. Rosecký, M. Sühring, M. Belda, V. Fuka, T. Halenka, and P. Huszár, *Validation of the PALM model system 6.0 in a real urban environment: a case study in Dejvice, Prague, the Czech Republic.* Geoscientific Model Development, 2021. **14**(8): p. 4797-4842.